Postprint of: Sobaszek M., Siuzdak K., Ryl J., Sawczak M., Gupta S., Carrizosa S., Ficek M., Dec B., Darowicki K., Bogdanowicz R., Diamond-Phase (Sp^3-C) Rich Boron-Doped Carbon Nanowalls (Sp^2-C): A Physico-Chemical And Electrochemical Properties, Journal of Physical Chemistry C, Vol. 121, Iss. 38 (2017), pp. 20821-20833

Diamond-phase (sp^3-*C*) Rich Boron-Doped Carbon Nanowalls (sp^2-*C*): A Physico-Chemical And Electrochemical Properties

M. Sobaszek[a], K. Siuzdak[b], J. Ryl[c], M. Sawczak[b], S. Gupta[d], S. B. Carrizosa[e], M. Ficek[a], B. Dec[a], K. Darowicki[c] and R. Bogdanowicz[a*]

[a] Department of Metrology and Optoelectronics, Faculty of Electronics, Telecommunications and Informatics, Gdansk University of Technology, 11/12 G. Narutowicza St., 80-233 Gdansk, Poland

[b] Centre for Plasma and Laser Engineering, The Szewalski Institute of Fluid-Flow Machinery, Polish Academy of Sciences, 14 Fiszera St., 80-231 Gdansk, Poland

[c] Department of Electrochemistry, Corrosion and Materials Engineering, Faculty of Chemistry, Gdansk University of Technology, 11/12 Narutowicza St., 80-233 Gdansk, Poland

[d] Department of Physics and Astronomy, Western Kentucky University, Bowling Green, KY 42101 (USA)

[e] Department of Chemistry, Western Kentucky University, Bowling Green, KY 42101 (USA)

***Corresponding author:** E-mail: rbogdan@eti.pg.edu.pl (Robert Bogdanowicz); Tel.: +48-58-347-15-03; Fax: +48 58-347-18-48

Abstract. The growth of B-CNW with different boron doping levels controlled by the [B]/[C] ratio in plasma, and the influence of boron on the obtained material's structure, surface morphology, electrical properties and electrochemical parameters, such as -ΔE and k°, were investigated. The fabricated boron-doped carbon nanowalls exhibit activity towards ferricyanide redox couple, reaching the peak separation value of only 85 mV. The flatband potential and the concentration of boron carriers were estimated in the B-CNW samples using the Mott-Schottky relationship. It was shown that the vertically oriented carbon planes are characterized by p-type conductivity and very high hole-acceptor concentration (3.33×10^{23} cm^{-3} for a highly doped sample), which provides high electrical conductivity. The enhanced electrochemical performance of B-CNWs electrodes is an advantageous feature that can be applied in ultrasensitive detection or energy storage devices.

1. Introduction

For almost two decades, carbon nanowalls (CNW) have drawn a lot of interest from the scientific community [1]. Generally, CNW can be described as planar sheets grown vertically to the substrate. In 2002, Wu *et al.* [2] published one of the first reports on the fabrication of CNW via microwave plasma-assisted chemical vapor deposition. In 2004, Hiramatsu *et al.* [3] used radio-frequency plasma-enhanced CVD, with C_2F_6/H_2 and CH_4/H_2 as source gases, to grow vertically aligned and wave-shaped carbon nanowalls. Nowadays, CNW can be found in fuel cells [4], batteries [5], supercapacitors [6], or as field emission devices [7] and so on. On the other hand, Giorgi *et al.* [8] used Pt-modified CNW for the electrochemical oxidation of methanol, while Luais *et al.* [9] reported that CNW is a suitable material for electrochemical transducers.

The recent electrochemical studies on low-dimensional sp^3-bonded (sp^3 C) and sp^2-bonded carbon (sp^2 C) materials such as nanodiamond or graphene [10–12], respectively, show favorable charge transfer dynamics at the basal plane and the edge plane sites which includes structural imperfections disrupting sp^2 C conjugation, nanoscale heterogeneity and surface corrugations. Also, it has been speculated that the sites with larger defect density, interfaces and rare surface sites (edge sites) are quite electroactive due to higher surface energy than those of basal clean surface [10]. Therefore, the maximization of these electroactive sites has become an active area of research. The nanodiamond (ND) particles [13], on the other hand, in theory would not be useful as electrochemical electrode material since they are undoped and consist of insulating sp^3–C core with unsaturated bonding and sp^2–C surface shell. However, it was proposed that surface carbon-oxygen functionalities (ketones, esters, alcohols and carboxyl), defect sites, and unsaturated bonding in ND give rise to the surface electronic states with energies within the bandgap of undoped diamond envisaging both an excess of unpaired electrons and unfilled electronic states [14].

Boron-doped carbon nanowalls attract attention owing to their tunable band gap, high conductivity, high mechanical robustness, high optical absorbance and other remarkable properties. Thus, our recent reports [15,16] present the successful use of B-CNWs for electrochemical detection of DNA purine bases or for laser desorption/ionization of small compounds (e.g. fatty acids, lipids, metabolites, saccharides and peptides) and their subsequent detection by mass spectrometry (LDI-MS).

In the present study, we investigated the growth of B-CNW with different doping concentrations (1.2k, 2k and 5k ppm of [B]/[C] ratio), and the influence of boron on the obtained material's structure, surface morphology, electrical properties and electrochemical parameters,

such as like -ΔE and k°. To the best of our knowledge, the effects of increasing boron level during B-CNW growth in a microwave plasma have not yet been reported. The addition of boron to the composition of gas mixture not only enhances the electrical or electrochemical properties, but also influences the structure of CNW by changing it from the mazelike to a heterogeneous distribution of nearly straight walls. It should be noted that only a small fraction (~0.2%) of boron acceptors is ionized at room temperature due to high bonding energy. The level of boron dopant in diamond reaches ca. 2×10^{20} atoms cm^{-3}, which results in a transition from p-type semiconducting to semi-metallic [17–19], where the current conduction is dominated by temperature-independent carrier concentration with mainly nearest-neighbour hopping conduction [20]. These high boron concentrations significantly change the crystalline structure, carbon phase composition and surface morphology of diamond [21].

In order to understand the B-CNW growth process, we conducted extensive comparative studies consisting of optical and electrical measurements. The main species present in the microwave plasma were investigated by optical emission spectroscopy (C_2, CH, BH, H_x and H_2). The surface morphology was analyzed by means of scanning electron microscopy, while the composition of as-prepared, pristine B-CNW films was studied by X-ray photoelectron spectroscopy (XPS), Raman spectroscopy and Laser Induced Breakdown spectroscopy (LIBS). The electrochemical properties of the B-CNW electrode were verified using electrochemical techniques, such as cyclic voltammetry and electrochemical impedance spectroscopy, performed in a standard three-electrode assembly. Moreover, an advanced electrochemical technique was used, namely, scanning electrochemical microscopy (SECM) to probe the surface of the samples. The surface states act as both electron donors and acceptors, and support catalytic redox processes in the presence of redox-active molecules via reduction and re-oxidation (feedback) mechanism. As a result, combining sp^3 C with sp^2 C phases at optimal concentration and configuration should result in the facile ion diffusion (D) and faster kinetic rate (k) transfer distribution depending on the interaction sites [22,23].

2. Experimental

Electrode growth: B-CNW were synthesized using the MWPECVD system (SEKI Technotron AX5400S, Japan). The base pressure inside the chamber was 10^{-4} Torr. Several B-CNW films have been fabricated using the following process conditions: gas mixtures — H_2, CH_4, B_2H_6 and N_2 with a total flow of 328 sccm; process pressure of 50 Torr; microwave power up to 1300 Watts; microwave radiation of 2.45 GHz; and the growth time adjusted to achieve a similar film

thickness of ca. 3.2 μm for each sample. All samples were doped by using diborane (B_2H_6) as an acceptor precursor. The [B]/[C] ratios in the plasma were set to 1.2k, 2k and 5k ppm, which resulted in the various contents of boron incorporated into nanowalls. Thus, the batch of samples was coded as B-CNW-1.2k, B-CNW-2k and B-CNW-5k. The time of growth was 4, 7 and 6h for B-CNW-1.2k, B-CNW-2k and B-CNW-5k, respectively. During the process, the substrate holder was heated up to 700°C by an induction heater, which was controlled by a thermocouple. B-CNW thin films were grown on (100)-oriented silicon substrates. Prior to CVD growth, Si substrates were seeded by spin-coating in the diamond slurry[24]. Previously, we have shown that seeding procedure yields high seeding densities in the range up to 10^{10} cm^{-2} [24].

Surface Morphology: Scanning Electron Microscope (SEM) FEI Quanta FEG 250 using 10 kV beam accelerating voltage with SE-ETD detector (secondary electron - Everhart-Thornley detector) working in high vacuum mode (pressure 10^{-4} Pa) was used to observe the structure of the B-CNW surface. The morphology studies were performed by means of optical microscopy with a 20× objective magnification and numerical aperture 0.4, and the program for data visualization and analysis (Gwyddion, 2.40, Czech Republic).

Optical emission and Raman spectroscopy: The emission spectra were recorded with a 0.3 m monochromator (SR303i, Andor) equipped with a 1200 groves/mm grating and ICCD detector (DH740, Andor). Optical emission was collected from the plasma volume about 3 mm above the substrate surface. Radiation was focused with the quartz lens and transmitted by the fused silica fibre to the spectrometer. The structures of the deposited films were studied by means of Raman spectroscopy using micro Raman system (InVia, Renishaw, UK) equipped with 514 nm argon-ion laser as an excitation source in combination with a 50 × objective magnification (NA = 0.5) and a 50 μm confocal aperture. Spectra were recorded in a range of 200–3500 cm^{-1} with an integration time of 5 s (10 averages).

X-Ray Photoelectron Spectroscopy (XPS) analysis was performed with Escalab 250Xi (ThermoFisher Scientific, United Kingdom) equipped with a monochromatic Al X-Ray source. High resolution spectra were made at a pass energy of 10 eV, and energy step size of 0.1 eV. The size of X-ray spot was 250 um. To provide in-depth analysis, the sample surface was etched by means of the ion gun (Ar^+, 3000 eV, 800 μm raster size). The estimated sputter rate of Ta_2O_5 was 2.24 nm/s, while the etching length was 240 s. In order to normalize the spectroscopic

measurements, the X axis (binding energy) of XPS spectrum was calibrated for the peak characteristics of neutral carbon C1*s* (284.6 eV).

Laser Induced Breakdown spectroscopy (LIBS): LIBS spectra were recorded using laboratory build system consisting of Nd:YAG laser (Briliant B, Quantel, France) used as an excitation source for laser ablation. The detection of plasma emission was realized by means of a 0.3 m monochromator (SR303i, Andor, United Kingdom) equipped with a 1200 groves/mm grating and ICCD detector (DH740, Andor, United Kingdom). The laser beam (1064 nm, 6 nm pulse duration) was focused on the sample surface by means of quartz lens (f=300 mm). For B-CNW films of 5 um in thickness, the laser beam energy was tuned to optimize the ablation rate and LIBS signal. LIBS spectra were averaged based on 100 measurements recorded for each sample. To avoid the influence of the laser, the sample was moved after each laser pulse by a distance comparable to the laser beam spot diameter, i.e. 100 μm, and the spectrum for the untreated sample area was also recorded.

Electrochemical evaluation: Characterization of the working electrode via electrochemical techniques (cyclic voltammetry and electrochemical impedance spectroscopy) was performed by means of the potentionstat-galvanostat system AutoLab PGStat 302N in a standard three-electrode assembly at 295 K. The Si substrates covered with B-CNW containing different boron concentrations were applied as a working electrode. For the electrochemical studies, the specimen holder was made from Polyether ether ketone material. It enabled contact between the limited geometric electrode surface and the electrolyte. The diameter of the round sample area wetted by electrolyte was 4 mm, giving the wetted area of 0.1256 cm^2. The counter electrode consisted of Pt gauze, while the reference electrode of Ag/AgCl/3 M KCl. The working electrode was not pretreated prior to electrochemical measurements. The electrodes were tested by cyclic voltammetry at different scan rates in the solution of 0.5 M K_2SO_4 without and with 5 mM $K_3Fe(CN)_6$. The electrochemical impedance spectroscopy technique was used to study B-CNW electrodes immersed in 0.5 M K_2SO_4 in the potential range from +0.7 V towards -0.2 V with a step of 50 mV, e.g. at 0.7, 0.65, 0.6, etc. The spectra were measured in the frequency range from 20 kHz to 0.1 kHz with an amplitude of 10 mV. Prior to impedance spectra recording, the electrode was conditioned at the fixed potential value for 5 min. All the electrolytes were purged with argon for 50 min. An Ar-cushion was kept above the electrolyte before the electrochemical test and during the measurement procedure.

Scanning electrochemical microscopy (SECM): The SECM measurements in terms of cyclic voltammetry, probe approach in feedback mode and microscopy were carried out using a bipotentiostat-galvanostat (CH Instruments Inc. Model 920D, Austin, TX). A saturated calomel electrode Ag/AgCl (3M KCl) and Pt wire of 1 mm diameter were used as the reference and counter electrodes, respectively. The carbon nanowall films were used as the working electrode. CV was performed in 0.5 M K_2SO_4 aqueous electrolyte within the potential range between –0.6 V and +0.4 V at room temperature and at a scan rate of v = 10 mV/s. In the case of SECM, we used a Pt microelectrode (~5 μm in diameter) encased in glass sheath, as the probe working electrode (tip), and 5 mM $K_3Fe(CN)_6$ and 5 mM FcMeOH as redox mediators in the supporting electrolyte (0.5 M K_2SO_4) for detecting kinetic differences. FcMeOH has a standard potential of E^0 = +0.21 V vs. Ag/AgCl, which is similar to that of $K_3Fe(CN)_6$. The Pt tip electrode was held at a potential of V_t = +0.5 V to ensure complete diffusion-limited oxidation of Fe(II) species originally present in the electrolyte solution to Fe(III). For SECM imaging, both the electrodes were biased, i.e. V_t = –0.5 V and V_S = +0.4 V to ensure complete reduction of the species generated at the tip. The tip was rastered over the working electrode surface area (250 μm x 250 μm) at a constant tip-substrate separation of ≤ 10-30 μm to generate a feedback image with an approximate resolution of tip radius with sub nanoampere tip current (i_T) sensitivity. The probe approach curves were fitted, and SECM maps were generated using Origin software (ver. 16.0).

3. Results and Discussion

3.1 The mechanism and structure of B-CNW growth

In order to reveal the CVD growth mechanism of B-CNW, the plasma optical emission spectra, collected during the deposition process of B-CNW with various boron [B]/[C] ratios in the gas phase, were analyzed (see **Figure 1B**). The recorded emission spectrum of plasma (B-CNW-1.2k sample) was contrasted with the plasma emission observed during the standard boron-doped diamond growth (BDD with [B]/[C] = 10k ppm) and illustrated in **Figure 1A**. The presence of intensive N_2 band at 358 nm ($C3\Pi_u \rightarrow B3\Pi_g$), and CN bands at 386 nm ($B^2\Sigma^+ \rightarrow X^2\Sigma^+$) and 418 nm confirms a significant contribution of nitrogen-originated species in the plasma. The presence of nitrogen species alters the plasma chemistry by changing the concentrations of important growth species, e.g. C_2 or CH (C_2 Swan bands (d→a)(Δv=0) at

516.5 nm; CH line ($A^2\Delta \rightarrow X^2\Pi$) at 431.4 nm), and playing a main role in the formation of diamond and graphitic phases in nanowalls.

The intensity ratios of C_2 band at 516.5 nm related to H_β lines equal to 0.41 and 0.66 for BDD-10k and B-CNW-1.2k processes, respectively. This clearly indicates the generation of C_2 in plasma due to the addition of nitrogen during the B-CNW deposition process. The C_2 adsorbates are the source of single carbon species that build the structure, or 'nucleate' the next layer of growing B-CNW. Increased concentration of C_2 species prefers the nucleation of sp^2 nanowall phase rather than the standard polycrystalline sp^3 diamond phase. Zhu *et al.* reported that strong C_2 emission could be an initiator of degraded quality of CVD diamond film [25].

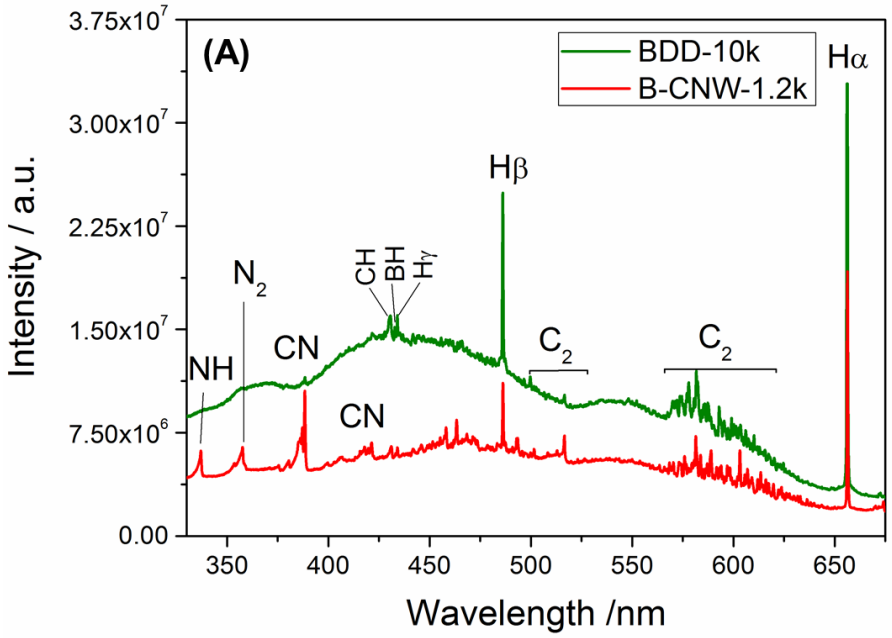

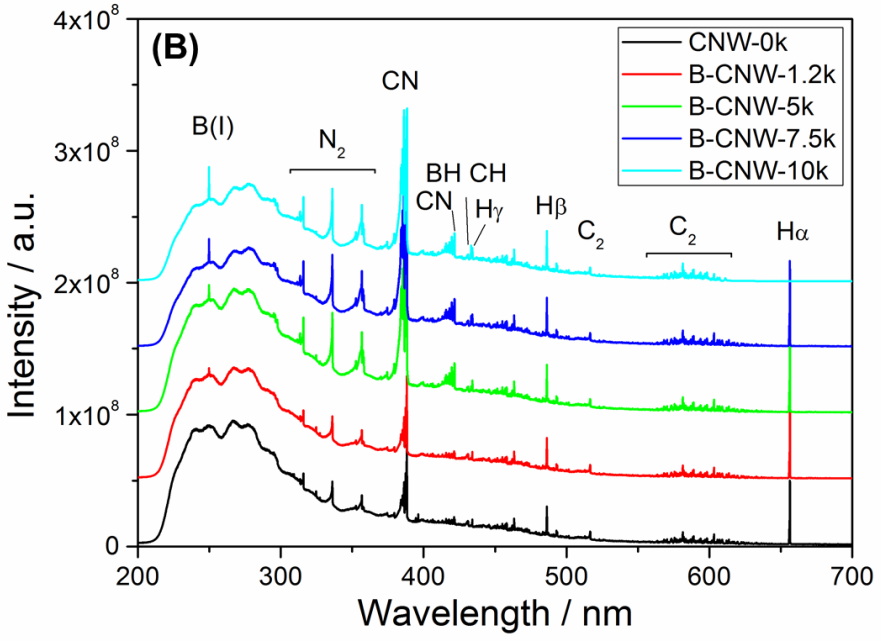

Figure 1. Optical emission spectra of microwave plasma recorded during the PECVD growth of: (A) BDD with 10k ppm [B]/[C] and B-CNW with 1.2k ppm [B]/[C]; and (B) B-CNW with various [B]/[C] ratios in the gas phase.

Nevertheless, the H_β -related CH line reveals a decrease down to 0.64 and 0.59 for BDD-10k and B-CNW-1.2k processes, respectively. The substantial quenching of CH levels is attributed to the formation of HCN and CN. Both compounds lower the availability of methyl radicals for growth of the next layer of nanowall [26] (see **Figure 4**).

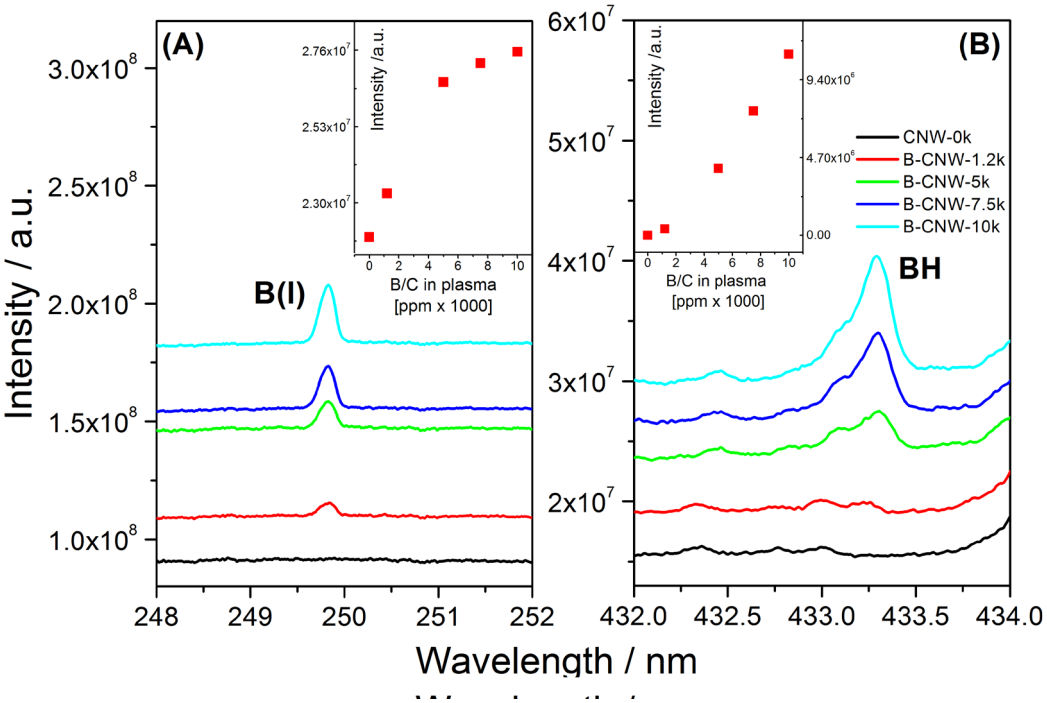

Figure 2. Optical emission spectra of microwave plasma depicting (A) B band (32S→22P), and (B) P, Q and R branches for (0,0) BH $A^1\Pi - X^1\Sigma^+$ transitions.

The plasma chemistry of boron precursor, i.e. diborane (B_2H_6) was studied to understand the high-efficiency doping of B-CNWs. The B (3^2S->2^2P) and BH ($A^1\Pi - X^1\Sigma^+$) bands, the most representative fingerprints of boron in plasma, have been studied and illustrated in **Figure 2**. The diborane admixture in plasma leads to the appearance of features in the spectra which are related to BH and B emissions, where BH emission is much stronger. The emission of B appeared at 249.8 nm (**Figure 2A**), while the presence of BH was recorded at 433 nm (**Figure 2B**). Both spectra clearly show the elevated band intensities in response to higher diborane

admixture in the plasma (**insets in Figure 2**). These increased intensities result in differences in the dissociation mechanism of boron hydrides. The BH lines in **Figure 2B** were observed in the spectral range of 432 – 436 nm, where the most intense (0,0) $A^1\Pi - X^1\Sigma^+$ transition appears in the well-resolved P and R branches and unresolved Q branch [27]. The intensity of R branch, with a maximum at 432.8 nm, dominates and it is well defined for the plasma process conducted at the highest boron concentration (10k ppm; **Figures 1, 2**). The R branch partially overlaps the less intense Q branch, which probably results from the insufficient resolution of spectrometer and does not allow determining the temperature from Q branch as proposed in the paper [27]. The intensity of BH emission increases with increasing [B]/[C] ratio in plasma, while it clearly disappears in the undoped CNW-0k film (see inset in **Figure 2B**). Thus, we conclude that the high content of BH species plays a main role in the doping process of CNW. Generally, BH_x species could be bound to the radical sites of the diamond {100} surface, forming stable complexes [28]. This finding will be discussed further in the next section.

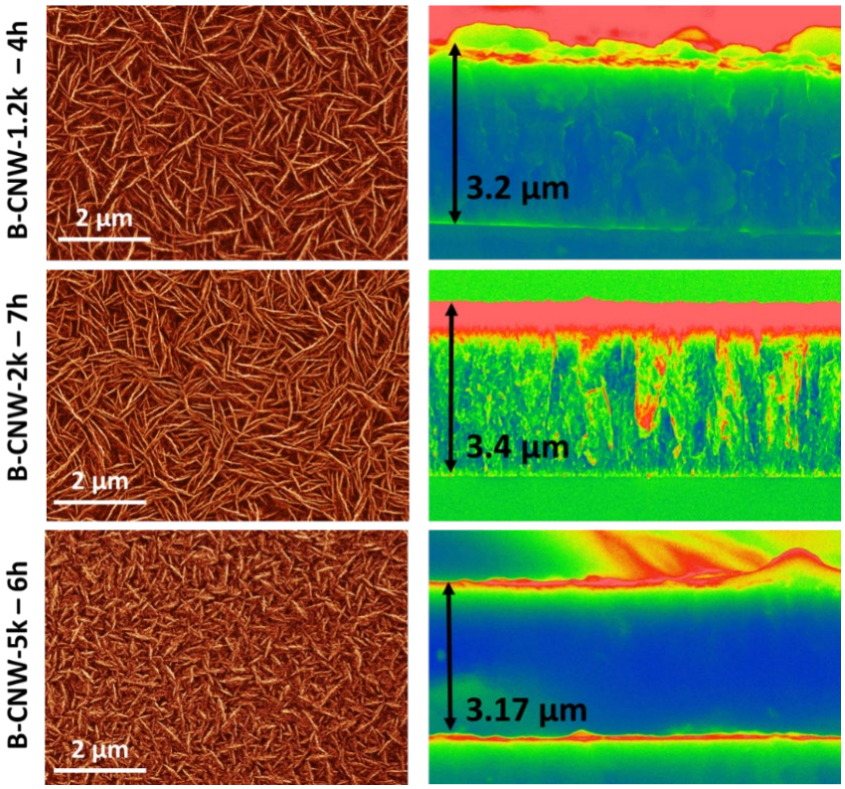

Figure 3. The HR-SEM images of B-CNW vs. various boron doping levels ([B]/[C] of 1.2k, 2k and 5k ppm): (left) top-view morphology, and (right) cross-sectional micro-images with marked wall thickness.

High-resolution scanning electron microscope was used to investigate the morphology of deposited samples. The left hand side images in **Figure 3** show the surface morphology of the obtained B-CNW samples. For all samples, the deposited walls are nearly straight, which is a different outcome than maze-like CNW reported by others. As can be seen, the presence of boron had a significant impact on the length and quantity of walls. In the case of sample B-CNW-1.2k, the average wall length was approximately 1.5 µm. The wall length decreased with increasing boron level in the gas phase, reaching the value of < 500 nm for B-CNW-5k sample. At the same time, the quantity of walls resulted in a denser film, e.g. B-CNW-5k sample. This can lead to increased specific capacitance due to the increasing amount of small pores between the nanowalls. On the other hand, the presence of boron also affects the film thickness (right panel in **Figure 3**). In order to achieve the same thickness in films with different doping levels, the deposition time has to be highly varied. Even a small change in the gas phase can almost double the deposition time. This phenomenon demonstrates the direct impact of boron atoms on growth kinetics during the MWPECVD process. The growth process of CNW in the presence of nitrogen involves H, CH_x, and CN radicals [1]. Wu *el al.* [29] proposed that a strong lateral field causes the lateral connection of tubular structures, and the formation of continuous wall. Hiramatsu *et al.* [30] suggested that carbon species nucleate to form nanoislands, which develop laterally into disordered flakes, and later into continuous walls. This description is in agreement with our observations presented in **Figure 4B**. Shang *et al.* [31] observed the anisotropic growth of nanorods into nanoflakes. While the growth mechanism of surface-bound CNW is still subject to modification, these reports could not explain the growth phenomenon of B-CNWs observed in our experiments.

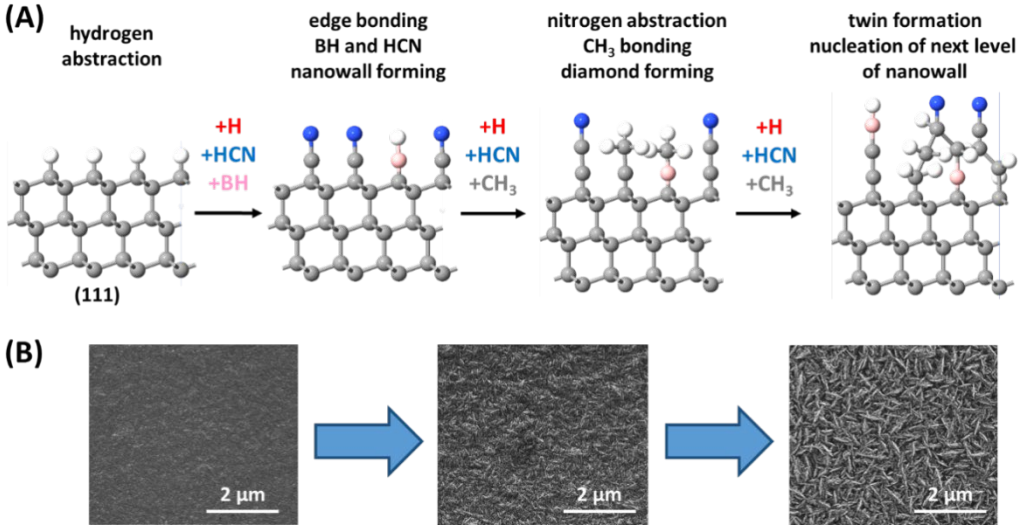

Figure 4. The scheme of (A) the most favorable growth mechanism of boron-doped carbon nanowalls in the microwave plasma; (B) SEM micro-images revealing the morphology of the subsequential steps of nanowall growth.

In the case of boron-doped CNW, BH_x radicals appear in the gas phase. The radicals may replace carbon or CN molecules because they are located at the grain boundaries or top edges of nanowalls. Hence, the modified scheme for the growth mechanism of B-CNW was proposed as follows (see **Figure 4A**):

(I) surface-bonded hydrogen abstraction;
(II) nanowall edge bonding of BH and HCN towards the nanowall formation process;
(III) nitrogen abstraction via CH_3 bonding towards the diamond formation mechanism;
(IV) twin formation nucleation of the next layer of nanowall.

This scheme is in agreement with other previous findings, such as [26,32] , and the results supported by the SEM micro-images or XPS cross-sectional studies presented in this paper. Generally, CN, H_yCNH_x, BH^-_x and CH^+_x radicals are jointly responsible for both plasma and surface reactions. H_yCNH_x originates from the reactions that involve hydrogen and methane species in plasma. The molecular geometry and higher electron−ion recombination rates of H_yCNH_x species could be responsible for the described edge growth of carbon nanowalls. Next, HNC-C bonding has the lowest bond energy in that system, i.e. 389 eV. The mechanism of H abstraction on the growth surface will be enhanced in the presence of nitrogen, as revealed by Yiming *et al.* [33]. This finding could also provide the way to grow graphene and graphitic wall-like structures.

Moreover, BH_x radicals are mainly responsible for the morphology development in B-CNW samples (see **Figure 3**). Low boron concentrations in the gas phase resulted in the micrometric length of nanowalls, while high boron levels induced their significant shortening. The strong morphological influence of BH_x is mainly attributed to the re-nucleation and twinning surface processes, as illustrated in **Figure 4A**. The twinning mechanism might originate from the formation of a boron rich cluster on a local {111} surface morphology, which also serves as a nucleus to the next layer of growth [26]. The boron incorporation level in diamond lattice was confirmed by the correlation of its composition in the gas phase (see Figure 2) with the boron content as determined experimentally by LIBS or XPS (**Figures 6 and 7**). The re-nucleation processes that shorten the walls are a positive effect, resulting in the higher specific surface

area. On the other hand, larger boron concentrations produce more carriers/acceptors enhancing electrochemical performance of nanowalls, as will be shown later on.

The Raman spectra recorded for B-CNW samples are presented in **Figure 5**. In all Raman spectra, two main bands were observed near 1350 and 1580 cm^{-1}, which respectively correspond to D band activated by lattice disorder resulting from the finite crystalline size, and G band indicating E_{2g} mode of graphite [34,35]. Additionally, the weak band near 1615 cm^{-1} is attributable to D' band [36]. The occurrence of D' band is characteristic for relatively low disorder structures such as graphite-like carbons and glassy carbon, but cannot be observed for high disordered forms of carbon, e.g. carbon black [37]. The peak positions and FWHM of D, G and D' bands determined by fitting Lorentzian distribution are listed in **Table 1**. The obtained values are comparable with those reported by other authors for carbon nanowalls ca. 1 µm in length. However, the bandwidths determined for our samples were, in general, nearly two times higher compared to undoped nanowalls [38]. The intensity of D' band increased with increasing boron-doping level and deposition time. In the case of sample B-CNW-1.2k deposited in the shortest time (4 hr), the D' band has not been observed which can be attributed to the high level of disorder. The extension of the time of deposition resulted in the increased intensity of D' band (see **Figure 5**).

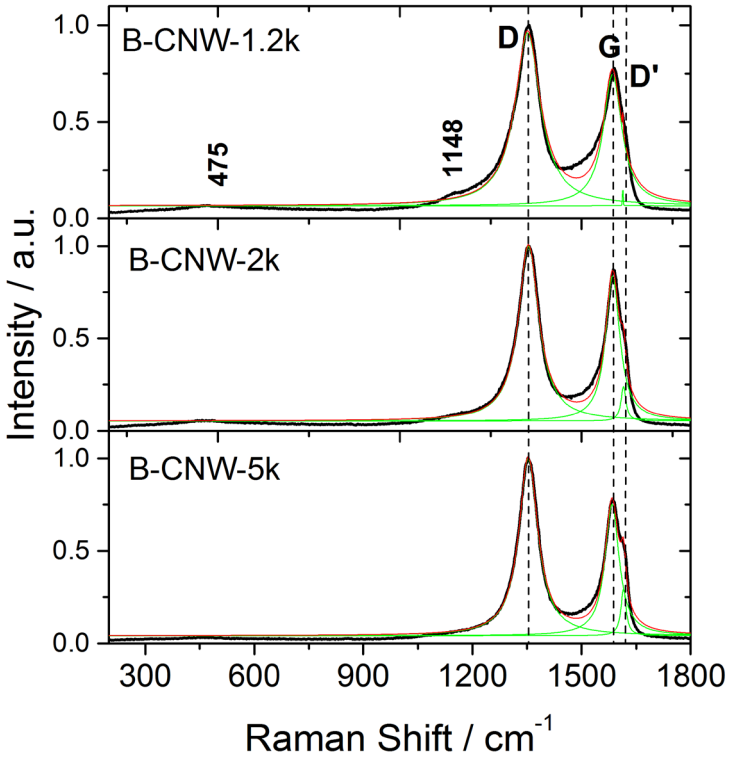

Figure 5. Normalized Raman spectra of B-CNW samples deposited at various [B]/[C] ratios in the gas phase, i.e. 1.2k, 2k, 5k ppm. The spectral decomposition was achieved by fitting Lorentzian distribution.

Table 1. The values of peak frequency (ν), bandwidth (W) and relative intensity (I_D/I_G) of D, G and D' bands in the Raman spectra of carbon nanowalls with different doping levels and deposition times, as determined from fitted Lorentzian function. Subscript letters D, G and D' denote parameters corresponding to D, G and D' bands, respectively.

Sample	Deposition time [h]	ν_D [cm^{-1}]	W_D [cm^{-1}]	ν_G [cm^{-1}]	W_G [cm^{-1}]	$\nu_{D'}$ [cm^{-1}]	$W_{D'}$ [cm^{-1}]	I_D/I_G [cm^{-1}]
B-CNW-1.2k	4	1351.7	85.2	1585.1	62.3	1615	-	1.3
B-CNW-2k	7	1354.7	68.8	1585.4	47.4	1615.1	16.2	1.2
B-CNW-5k	6	1353.5	63.9	1583.7	47.3	1615.2	16.8	1.3

The LIBS measurements were carried out on the B-CNW-1.2k, B-CNW-2k and B-CNW-5k samples deposited on silicon substrates for 4, 7 and 6 h, respectively (see **Figure 6**). The strong boron lines (249.7 and 249.8 nm) as well as the weak carbon line at 247.85 nm were observed in the emission spectra recorded in the narrow wavelength range. The emission in the spectral range of 250 – 253 nm originates from the silicon substrate. For the samples deposited in the shortest time, the nanowalls had been completely removed during a single pulse laser ablation process, which resulted in the bare silicon pattern in the plasma emission spectra. The relative boron-doping level, determined from the B/C line intensity ratio, equaled to 61.34, 66.70 and 80.43 for samples 1.2k, 2k and 5k, respectively. The linear relationship between the B/C ratio and boron concentration indicates that the doping level of carbon nanowalls is a linear function of B_2H_6 concentration.

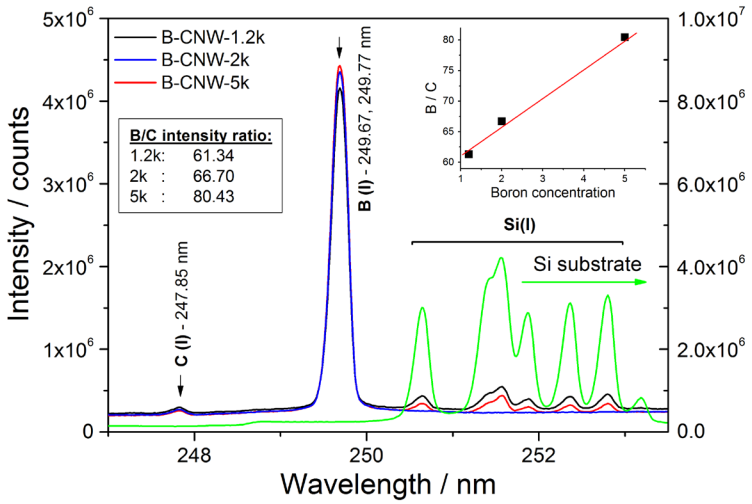

Figure 6. The LIBS spectra of bare silicon substrates and B-CNW samples with various boron concentrations ([B]/[C] equal 1.2k, 2k and 5k ppm) deposited by the MWPECVD process.

The XPS study of B-CNW samples with different boron dopant concentrations revealed subtle chemical changes between the analyzed sample surfaces (**Figure 7**). It has been found that the position of C 1*s* line shifted to lower binding energies upon boron doping, with the magnitude of the shift varying from 0.1 up to 0.3 eV. Five components were used for deconvolution purposes in high-resolution spectra in the C 1*s* energy range, as exemplified by [B]/[C] = 5k sample in **Figure 6**. The most notable components were located at BE of 284.5 eV and 285.1 eV, which corresponds to C-C sp^2 and C-C sp^3, respectively. Two additional components found at 286.5 eV and 288.4 eV were tentatively identified, and assigned to carbon bonds C-O/C-N and C=O, respectively. A significantly lower component at approximately 283.1 eV was attributed to the substitutional C-B configuration. The aforementioned values of binding energy are commonly found in literature [39–42].

It is also noteworthy that the share of oxygen and nitrogen, analyzed on the basis of O 1*s* and N 1*s* spectra, did not exceed 8 at.% in total. The presence of N 1*s* peak at 400.0 eV should be linked to miscellaneous C-N covalent bonds, such as -C-NH_2, -C=N or –C-N-C. The presence of B-N bonds, in the form of peak at 398.0 eV, has not been confirmed [42,43]. The concentrations of both oxygen and nitrogen increased with increasing B dopant concentration, which suggests a higher reactivity of the electrode. However, boron itself was not directly detected due to insufficient detection sensitivity of XPS system. The presence of boron could be revealed only because of its interaction with carbon.

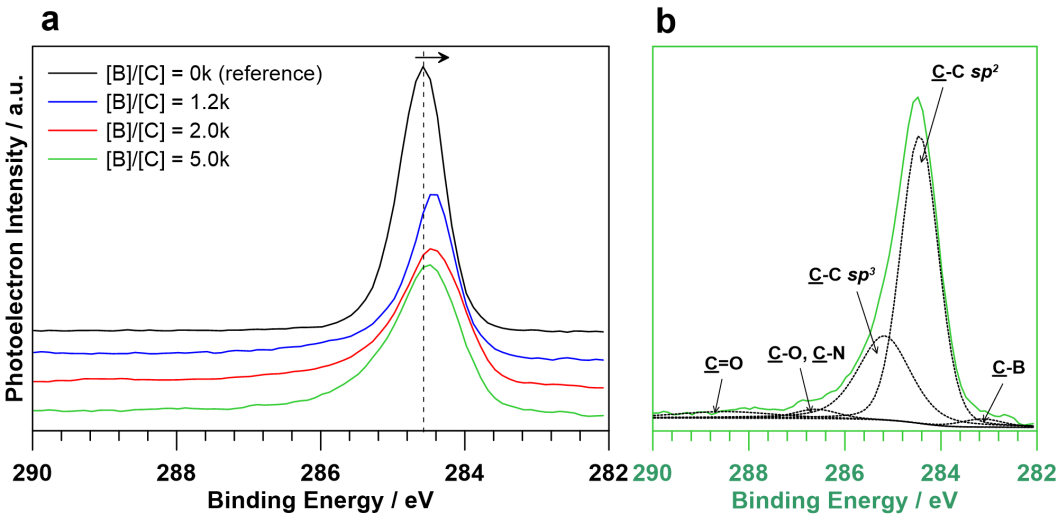

Figure 7. High resolution XPS spectra of B-CNW samples in the C 1*s* energy range; a) spectra registered for [B]/[C] doping ratios ranging from 1.2 to 5k, and the reference sample, b) spectra for [B]/[C] = 5k with the superimposed deconvolution peaks.

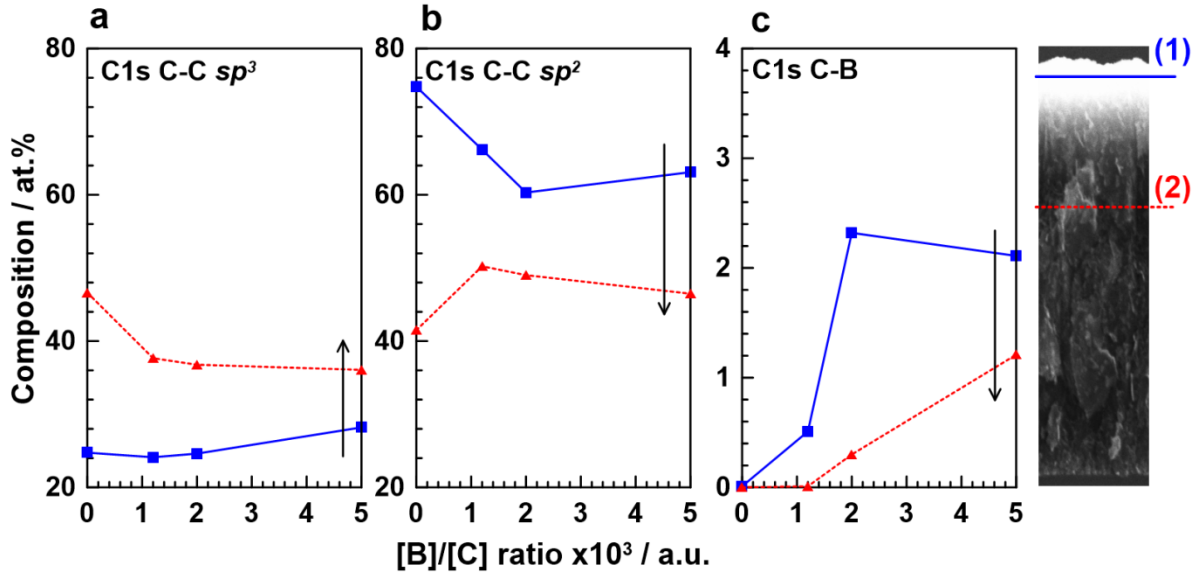

Figure 8. The influence of B dopant concentration and the depth of sampling on the chemistry of B-CNW electrodes. High resolution XPS analysis was carried out in the C 1*s* energy range, (1) before and (2) after Ar^+ ion sputtering for 240 s (3000 V); a) C-C sp^3 peak at 285.1 eV, b) C-C sp^2 peak at 284.5 eV, and c) C-B peak at 283.1 eV.

Figure 8 shows the variation in the chemistry of the analyzed electrodes as a result of deep Ar^+ ion beam etching (3000 V) for a period of 240 s. The depth profile analysis indicates the higher concentration of sp^3-carbon and lower concentration of sp^2-carbon, which corroborates the results of Raman spectra analysis. Moreover, it should be pointed out that the observed

difference is probably even more significant, since the peak located at 284.5 eV partially includes information on neutral carbon contamination from atmospheric air. These results may suggest that the nanostructures visible on the SEM cross-section micrographs and the XPS depth profile of B-CNW film are built of sp^3-carbon, which can affect the local electric properties. The intensity of deconvoluted peak located at 283.1 eV indirectly indicates a decrease in boron concentration within the electrode volume and boron accumulation on the electrode surface. This is in good agreement with simultaneous decrease in sp^2-carbon concentration. Therefore, it could be assumed that the electrode conductivity is highly surface-dependent. The results of the peak deconvolution of each investigated component are summarized in **Table 2**. As in the case of boron, the presence of nitrogen revealed on the basis of N 1*s* spectra drops along the depth profile of the investigated material in samples lacking the lane or when the lane was below the spectrometer threshold.

Table 2. High-resolution XPS analysis of different carbon C1*s* chemical states in B-CNW-1.2k, B-CNW-2k and B-CNW-5k samples (1) at the sample surface and (2) along the depth profile using ion gun sputtering.

Chemical state	Sampling depth	Binding Energy [eV]	[B]/[C] ratio in ppm ×1000			
			0	1.2	2	5
C-C sp^2	Surface (1)	284.5	74.7	66.2	60.3	63.1
	Depth profile (2)		41.5	50.2	49	46.4
C-C sp^3	(1)	285.1	24.8	24.1	24.6	28.2
	(2)		46.6	37.7	36.8	36.1
C-B	(1)	283.1	0.0	0.5	2.3	2.1
	(2)		0	0	0.3	1.2
C-O / C-N	(1)	286.5	0.2	4.8	4.9	2.4
	(2)		5.2	5.6	6.4	5.8
C=O	(1)	288.4	0.3	4.4	7.9	4.2
	(2)		6.7	6.5	7.5	10.5

3.2 Electrochemical characterization of B-CNW

Despite the fact that the procedures for CNW fabrication have been available for long time, the electrochemical studies of carbon nanowalls are still very scarce. Until now, the electrochemical characterization of CNW doped with different boron levels has not been published. In order to examine the differences in the electrochemical activity of materials fabricated at different diborane concentrations in the gas mixtures, the cyclic voltammetry and electrochemical impedance spectroscopy techniques were applied. **Figure 9** shows the cyclic voltammetric

behavior of boron-doped carbon nanowall electrodes in the range from -1.2 to +1.4 V *vs.* Ag/AgCl/3M KCl at a scan rate of 50 mV/s in 0.5 M K_2SO_4 (pH 7) without any additives. As it can be observed, the lowest background current was registered for B-CNW-1.2k sample, yielding the potential window of 2.6 V. With increasing diborane concentration in a synthesis mixture, the B-CNW samples exhibited higher capacitive current. This finding could be related to the analysis of HR-SEM, wherein the densest film is observed for B-CNW-5k resulting from the walls shortening. The amount of small pores between nanowalls increases and contributes to the specific surface area increasing. Furthermore, the larger boron concentration produces more carriers/acceptors and as was confirmed via XPS depth profile inspection the accumulation of boron is mainly located at the electrode surface. Therefore, increase of surface roughness and the area available for electrolyte ions penetration along with the improved sample conductivity significantly impact onto the charging current and thus the highest one is observed for B:CNW-5k.. Simultaneously, the current in the cathodic and anodic regimes increased rapidly which led to narrowing of the potential window down to 2 V and 1.4 V for B-CNW-2k and B-CNW-5k, respectively. Furthermore, the CV testing of B-CNW-5k sample showed additional oxidation and reduction peaks. As it was revealed within XPS analysis, the concentration of oxygen and nitrogen increases with the increasing boron concentration influencing the material reactivity and the presence of sp^2 phase was confirmed (see also Raman spectra in Fig. 5 and Table 1). Thus, the signal near +1.0 V vs. Ag/AgCl/3M KCl could be ascribed to the oxidation of sp^2 rich sites whereas the activity in the cathodic regime may be ascribed to the oxygen reduction reaction (ORR) as it was revealed for boron doped diamond containing non-diamond carbon [44]. Since incorporation of non-diamond carbon (sp^2) occurs predominantly at the grain boundaries[44] , its presence will be mostly marked in the case of B:NCD-5 sample that is composed of the shortest walls and possess the highest roughness among all the investigated materials. Due to that, binding sites for oxygen are available and ORR becomes possible. For pure BDD substrate, such redox activity is not observed[45] that is due to the low surface potential resulting from low surface oxides/oxygen functionalities. In the next step, the B-CNW electrode materials were tested in a solution containing ferro/feriicyanide probe, which stays as an outer sphere redox system that is surface sensitive [46]. In **Table 3**, the localization of oxidation (E_{ox}) and reduction peaks (E_{red}) as well as the values of separation for both potentials labelled as ΔE have been collated. The ΔE gradually decreases down to 98 and 85 mV for B-CNW-1.2k and B-CNW-5k, respectively. As can be noticed, the ΔE value is higher than the predicted value of 59 mV. This results from the occurrence of slow electron transfer kinetics at the CNW electrode surface or can be caused by the resistivity of CNW layer

grown by the CVD process [47]. Nevertheless, the peak separation values for the fabricated samples towards $[Fe(CN)_6]^{3-/4-}$redox system are very similar to those of a few undoped CNW electrode materials characterized electrochemically without any initial treatment, e.g. by electrochemical oxidation [48] , and much lower compared to other pristine CNW [49,50]. Such low value of ΔE results from the arrangement of sheets perpendicular to the Si substrate that facilitates electronic conduction through them and leaves a high number of exposed reactive edges, as shown in **Figure 3** containing the SEM images.

It is worth noting that the value of peak current does not follow an increase in diborane concentration in the gas mixture during the CVD process. Despite repeatable CV measurements, the lowest peak current density was registered for B-CNW-5k. Similar phenomenon was observed by Gonzalez *et al.* [51], in the CNW samples produced at three different Ar flows, which were electrochemically studied by using different polarization levels. Such behavior is sometimes attributed to the efficient penetration of feriicyanide ions into the nanostructure [52].

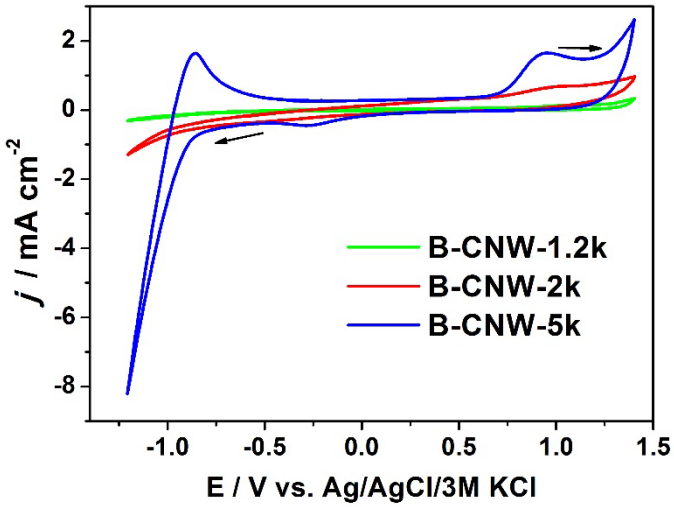

Figure 9. CV curves registered in 0.5 M K_2SO_4 with a scanning speed of 50 mV/s for the set of B-CNW samples with various boron concentrations.

The impedance spectra were registered in the potential range for which no faradaic processes occur (the presence of oxidation or reduction peak is not observed), while the electrode was immersed in 0.5 M K_2SO_4. The selected potential range covered the regime from +0.7 to -0.2 V *vs*. Ag/AgCl/3M KCl (marked in **Figure 10**). In such case, any Faraday activity does not contribute to the EIS spectrum, which simplifies the analysis of the obtained spectra. The collected spectra served as input for the Mott-Schottky approach that is frequently applied for the electrochemical characterization of semiconducting materials, including carbon-based

materials [53–55] , and allows the determination of carrier densities and flatband potential. The analysis was based on the assumption that the capacitance of the space charge layer is much lower compared to Helmholtz layer, and it depends on the type of semiconductor (n or p) [56]:

$$\frac{1}{C_{sc}^2} = \frac{2}{e\varepsilon\varepsilon_0 N}\left(\pm E - E_f - \frac{kT}{e}\right) \qquad (1)$$

where C_{sc} is the space-charge capacitance, ε is the dielectric constant of the semiconductor, ε_0 is the permittivity of the free space (8.85×10^{-14} F/cm), e is the electron charge (1.602×10^{-19} C), N is the donor or acceptor carrier densities (carriers/cm^3), E is the applied potential, E_f is the flatband potential, k is the Boltzmann constant and T stays for the absolute temperature.

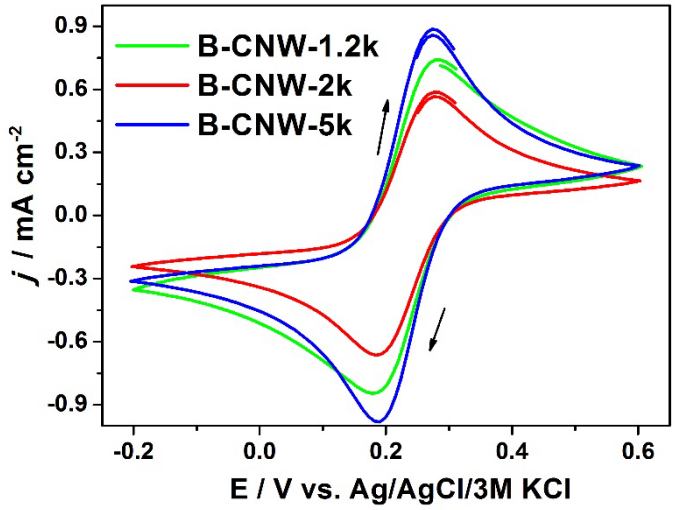

Figure 10. CV curves recorded for the macro-electrode (planar diffusion) in 0.5 M K_2SO_4 + 5 mM $K_3Fe(CN)_6$ at a scan rate of 50 mV/s.

Table 3. The values of oxidation (E_{ox}) and reduction potentials (E_{red}) and the resulting peak-to-peak separation (ΔE) for the CNW samples.

Sample	E_{ox} / V	E_{red} / V	ΔE / mV
B-CNW-1.2k	0.283	0.185	98
B-CNW-2k	0.279	0.187	92
B-CNW-5k	0.275	0.190	85

Moreover, the carrier density (N) and the flatband potential could be determined from the slope and extrapolation to $1/C_{sc}^2 = 0$ by using potentials applied to the electrode plotted versus $1/C_{sc}^2$ in Figure 11. The type of semiconductor can be identified from the slope of the Mott-Schottky plot under assumption that the positive slope indicates n-type semiconductor whereas the

negative slope is typical for p-type carrier conduction. The analysis of impedance spectra was performed on the basis of the capacitance of space charge layer resulting from the relation C = -1/(2π*f*Z") [57,58] , where Z" is an imaginary part of the impedance for selected frequency *f*. Based on the results presented in **Figure 11**, where the Mott-Schottky plot for different frequencies covering both high (14000 Hz) and low frequency (100 Hz) regions is shown, one can see that the influence of the frequency dispersion was not observed, which is usually attributed to the dielectric relaxation in the depletion layer or deep donor levels [59]. The same phenomenon was observed in the case of CNW samples labelled as B-CNW-2k and B-CNW-5k. Thus, in accordance with other reports [53,60,61] , the double layer capacitance of boron-doped carbon nanowalls samples was determined on the basis of the imaginary component of impedance spectra at the fixed frequency and by taking into account the geometric surface area. The Mott-Schottky plots obtained for different B-CNW samples are presented in **Figure 12**, while the determined values of flatband potential and carrier density are listed in **Table 4**. In the calculation of carrier density, the dielectric constant of 7 was used. This value was obtained from the theoretical approach applied to graphene ribbon edges [62]. Independently of diborane concentration in the gaseous synthesis mixture, all the Mott-Schottky plots exhibited a distinct negative slope, indicating p-type carrier conduction in the examined samples, as it was previously demonstrated for boron-doped diamond [58,63] or nanographene [64] , but with much lower resistivity (see **Table 4**). Since any similar data for boron-doped CNW have not yet been reported, a literature-based comparative analysis of the material fabricated by us is not possible. As it can be observed, with increasing boron concentration, the flatband potential value shifts towards higher anodic regime from 1.16 V *vs*. Ag/AgCl/3M KCl for B-CNW-1.2k up to 2.54 V *vs*. Ag/AgCl/3M KCl for B-CNW-5k. The similar values of E_f were determined for the modified multi-layered graphene [60]. Such a positive shift in E_f position indicates that the boron content strongly affects the interfacial electron energetics. Knowing that the flatband potential of p-type semiconductor is located in the close vicinity of the valence band [65], it can be hypothesized that the whole band offset, namely, the location of the conduction and valence bands, was modified upon boron doping [66].

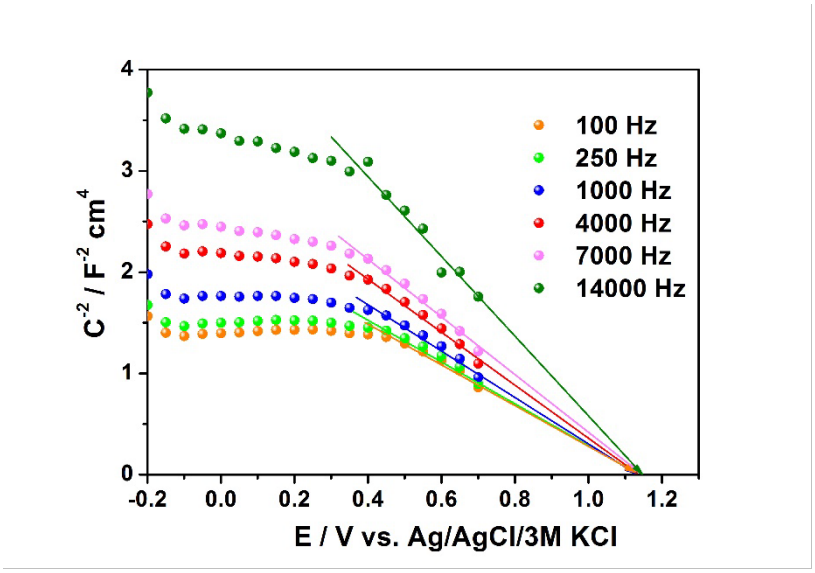

Figure 11. The Mott-Schottky plots for B-CNW-1.2k sample for different frequencies.

The same rising trend was observed when the acceptor concentration was analysed in terms of diborane amount in the CVD gas mixture, reaching the value of 3.33×10^{23} for B-CNW-5k sample. This demonstrates that the boron incorporation can greatly improve the electrical conductivity of the fabricated B-CNW samples. The estimated N_A values were much higher, and the resistivity was much lower in comparison to the values reported for boron-doped diamond [67,68]. That could have resulted from the surface properties, i.e. roughness and chemical composition (sp^2/sp^3 ratio, boron incorporation), cleanness of the surface as well as from the way of carrying out the electrochemical measurements (e.g. cell design, the distance between the working and reference electrodes).

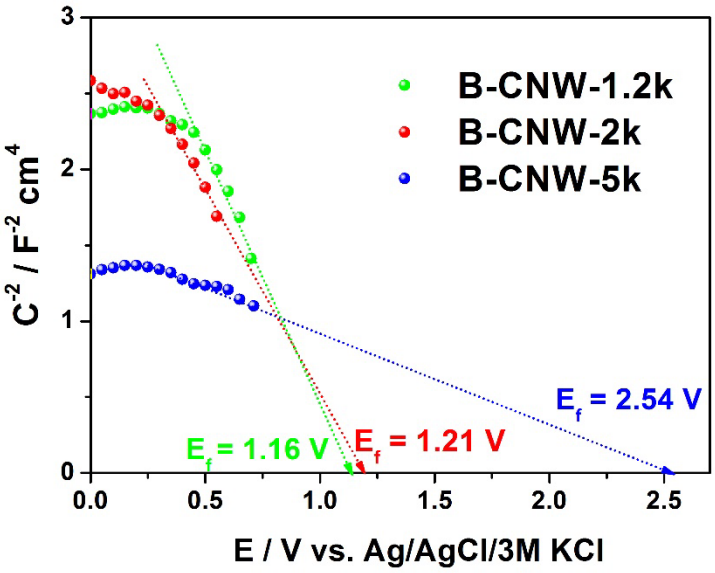

Figure 12. The Mott-Schottky diagrams of B-CNW samples vs. various boron doping levels along with estimated values of flat band potential (E_f).

Table 4. The estimated values of carrier concentration (N_A) at the boron-doped CNW in 0.5 M K_2SO_4 solution, and film resistivity studied with a four-point probe.

Sample	N_A / cm^{-3}	Resistivity (mOhm cm)
B-CNW-1.2k	6.21×10^{22}	4.2×10^{-3}
B-CNW-2k	7.59×10^{22}	1.5×10^{-3}
B-CNW-5k	3.33×10^{23}	4.7×10^{-4}

From the above discussion, it becomes imperative that we investigate the complex electrochemical processes in nano-structured carbon electrodes to probe local electron transfer/charge transport to correlate it with the molecular structure by using SECM [69,70]. The SECM studies of redox reactions occurring in close proximity to the electrode surface (probe approach mode) were used to obtain quantitative information about the local reaction rates. However, we also made CV measurements of microelectrode configuration, yielding the redox peak position and peak separation, as presented in **Figure 13** and **Table 5**. With increasing boron concentration, the electrochemical potential window becomes narrower, which is analogous to the results observed in the case of traditional macroelectrode configuration shown in **Figure 13**.

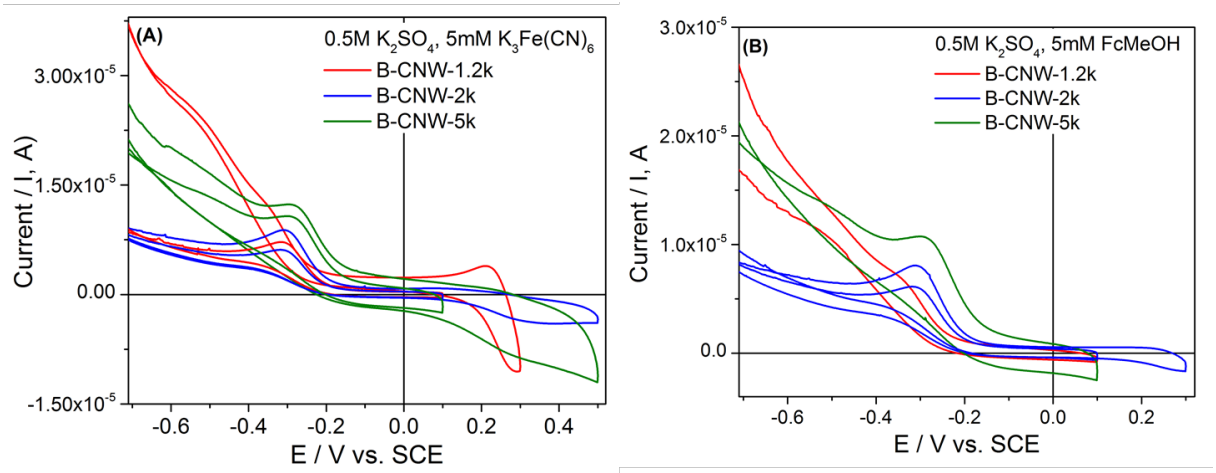

Figure 13. CV curves of microelectrode (convergent or hemispherical diffusion) configuration recorded in 0.5M K_2SO_4 with added (A) 5 mM $K_3Fe(CN)_6$, and (B) 5mM FcMeOH redox mediators at a scan rate of 10 mV/s

Thus, the dissociation of water molecules occurred at lower potentials with both redox mediators used. Moreover, in the case of microelectrode configuration, we occasionally

observed additional oxidation and/or reduction peaks that can be attributed to the higher electroactivity of surface functional groups at the local level. It should be mentioned that CV measured during SECM looks a bit different from traditional electrochemistry due to the size of the electrodes area exposed (microelectrode configuration, < 3 mm) and the hemispherical or convergent diffusion as opposed to planar diffusion in macro configuration. As for the voltammetry, we have included the best CVs measured using SECM.

Table 5. The estimated oxidation (E_{ox}) and reduction (E_{red}) potentials, and peak-to-peak separation values (**Δ E)** at the boron-doped CNW in $K_3Fe(CN)_6$ and (FcMeOH) solutions.

Sample	E_{ox} / V $K_3Fe(CN)_6$ (FcMeOH)	E_{red} / V $K_3Fe(CN)_6$ (FcMeOH)	Δ E / mV $K_3Fe(CN)_6$ (FcMeOH)
B-CNW-1.2k	0.312 (0.310)	0.230 (0.215)	82 (95)
B-CNW-2k	0.299 (0.340)	0.221 (0.255)	78 (85)
B-CNW-5k	0.280 (0.300)	0.205 (0.220)	75 (80)

Figure 14 provides probe approach curves in terms of normalized tip current versus normalized distance, L = d/a, where d is substrate (electrode)-tip distance and a, the radius of the tip. The tip electrode current (i_T) reaches plateau behavior with steady-state current following:$i_{T,\infty} = 4nFCDa$, where n is the number of electrons transferred at the electrode tip ($O + ne^- \rightarrow R$), F is Faraday constant, C is the concentration

of oxidized species, and D is the diffusion coefficient limited by hemispherical region. With tip approaching the surface of the heterogeneous electrode surface, the reduced species formed at the tip are oxidized at the conductive surface, yielding an increase in the tip current following ($i_T > i_{T,\infty}$, $i_T^c(L) = \frac{i_T}{i_{T,\infty}} = [k_1 + k_2/L + k_3\exp(k_4/L)]$) that creates a regenerative "positive" feedback loop. The opposite effect is observed when probing insulating region, creating a "negative" feedback loop that decreases the tip current [$i_T < i_{T,\infty}$, $i_T^{ins}(L) = \frac{i_T}{i_{T,\infty}} = 1/[k_1 + k_2/L + k_3\exp(k_4/L)]$, where k_1, k_2, k_3 and k_4 are coefficients depending on RG (ratio of insulating sheath radius to a, which is equal to 5) and normalized distance $L = d_o\text{-}d_{exp}/a$, (see **Table 6** for fitted values).

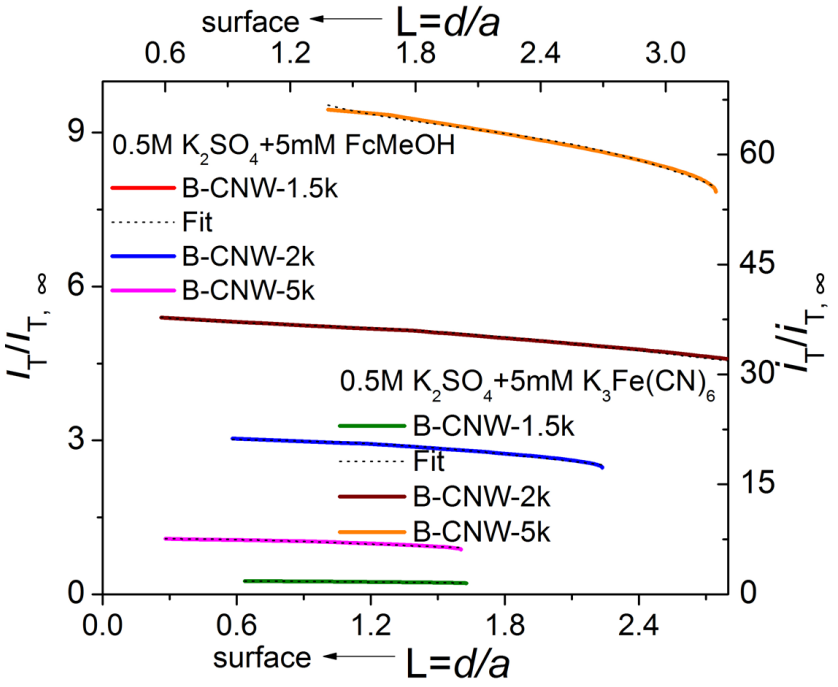

Figure 14. Probe approach curves obtained in 0.5 M K_2SO_4 as base electrolyte and 5 mM $K_3Fe(CN)_6$ and 5 mM FcMeOH redox mediators, with tip voltage V_{tip} = -0.5 V and substrate voltage V_{sub} = +0.4 V. The corresponding fitted functions are plotted as dashed lines.

The total tip current is given by: $i_T = 4\text{nFDCa} + \frac{\text{nFDC}}{d}\pi a^2$, where the symbols have their usual meaning. The diffusion (D) of redox species ranged from 3×10^{-11} to 7×10^{-10} m^2s^{-1} in the increasing order with increasing boron concentration for FcMeOH as opposed to $K_3Fe(CN)_6$ (2×10^{-12}–1.3×10^{-11} m^2s^{-1}). Similar behavior was observed for boron-doped diamond films or nanodiamond immobilized on the boron-doped diamond electrodes. The second term of the equation is reminiscent of the extent of concavity (or convexity) of probe approach curves plotted in **Figure 14** as dashed lines. In **Table 6**, the parameter values (k_1 parameter is usually considered to be the kinetic rate transfer) are provided with an accuracy of < 3%, which is smaller than typical experimental uncertainties. The parameters were determined by fitting d_o in L and by using different RG values for all the heterogeneous kinetics at the tip and diffusion-controlled mediator regeneration at the substrate samples studied. The feedback approach curve then represents a measure of the absolute distance when the electrode diameter and the ratio between the electrode diameter and the insulating glass sheath is known. The electron kinetic transfer rate (k_1) is faster with increasing boron concentration for FcMeOH in contrast to $K_3Fe(CN)_6$ redox probe.

Table 6. Summary of fitted parameter values for $K_3Fe(CN)_6$ (FcMeOH) redox mediators.

Sample	k_1	k_2	k_3	k_4	χ^2 (% Error)	Validity range
B-CNW-1.2k	0.477 (0.211)	0.061 (-0.004)	1.00 (1.00)	4.059 (16.97)	< 3	0.1-10
B-CNW-2k	0.028 (0.339)	-0.008 (-0.005)	0.059 (1.00)	9.020 (6.354)	< 3	0.1-10
B-CNW-5k	0.017 (0.937)	-0.003 (0.0045)	1.00 (1.00)	20.548 (2.896)	< 3	0.1-10

The visualization of electrochemical (re)activity or the mapping of adsorption sites density is performed in constant height feedback imaging mode by taking advantage of an amperometric tip current that originates from the redox mediator, modulated by variations in the tip-to-sample distance and by the local electrochemical activity of the sample surface. For example, on insulating or homogeneously active surface, variations in the tip current reflect variations in the sample topography. The variations in the tip ion current on electrode surfaces are indicative of variations in the local electrochemical (re)activity of the sample. Thus, changes in the electrochemical activity (electron rate transfer) give rise to changes in the feedback (tip) current. **Figure 15** contains the SECM images of a 250 × 250 μm^2 area as two-dimensional contour 'heat maps' and three-dimension maps, displaying the ion current distribution of the tip. First, the tip was polarized at potential sufficient for causing an electrochemical redox reaction, and then the current was recorded over the surface of polarized electrode. The redox reactions display occasional higher (peak)/lower (valley) values over the electrode surface areas which are characteristic of conductive/semiconductive or insulating behavior at the electrode/electrolyte interface. It is apparent from the probe current distribution that the samples yielded several regions of highly electroactive sites (hot spot sites) where the density distribution shows FWHM of approx. ~20–40 μm. This finding is comparable to the hemispherical diffusion boundary obtained with potassium. It is noteworthy that ferrocene methanol results in much smoother density distribution, with only occasional peaks/valleys observed in the plots.

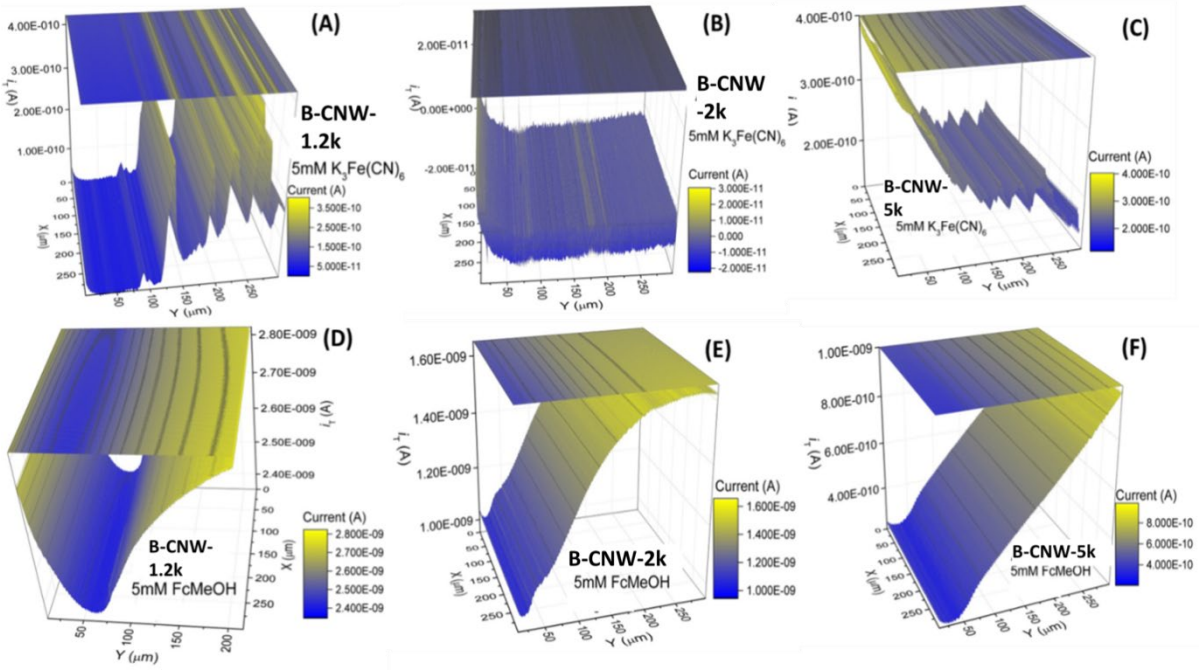

Figure 15. The SECM images of B-CNW samples taken in the 250 × 250 μm area. The images were obtained in 0.5 M K_2SO_4 as base electrolyte, with 5 mM $K_3Fe(CN)_6$ and 5 mM FcMeOH redox mediators in negative feedback mode. All samples displayed current distributions in 2-dimensional contour heat map and 3-dimensional space with higher (peak)/lower (valley or almost flat) current behavior. The color scale was used to plot the values of the probe current.

On the contrary, with increasing boron concentration, the kinetic transfer rate becomes faster for the neutral ferrocene methanol redox agent compared to potassium ferricyanide ions (**see Table 6**). These findings strengthen the multiple roles played by sp^2 C-rich carbon nanowalls with sp^3 C diamond phase in providing a robust interconnected topological conductive network, where point-like sites and surface functionalities associated with π-bonding and defect sites serve as favorable hybridized pockets.

Conclusions

In summary, the fabricated boron-doped carbon nanowalls exhibited the p-type semiconductor nature with an activity towards ferricyanide redox couple, reaching the peak separation value of only 85 mV. BH_x radicals were mainly responsible for the developed morphology of B-CNW samples. The low boron concentration in the gas phase resulted in micrometric length of nanowalls, while higher boron levels induced significant nanowall shortening. The strong

morphological influence of BH_x is mainly attributed to the re-nucleation and twinning surface processes.

The flatband potentials and concentrations of boron carriers were estimated in the B-CNW samples using the Mott-Schottky relationship. It was shown that vertically oriented carbon planes are characterized by p-type conductivity and very high hole-acceptor concentration (3.33×10^{23} cm^{-3} for B-CNW-5k sample), which provides high electrical conductivity.

As it was determined, an increase in diborane concentration in the synthesis mixture strongly shifts the flat band potential towards anodic regime, and increases the acceptor concentration. The application of SECM imaging supplied quantitative information on electrode kinetics, local charge transport behavior and the map of electrochemical redox activity i.e. higher/lower tip current distribution. The present study provides insights into physicochemical processes, and reinforces the role of nanoscale surface morphology and optimum sp^3 C/sp^2 C ratio that promote interphase/interfacial dynamics of physico-chemical processes.

Acknowledgments

The authors gratefully acknowledge financial support from the Polish National Science Centre (NCN) under Grant No. 2016/21/B/ST7/01430, 2016/22/E/ST7/00102, 2014/14/M/ST5/00715 and 2014/14/E/ST7/00104. The DS funds of the Faculty of Electronics, Telecommunications and Informatics of the Gdansk University of Technology. The author (S.G.) acknowledges NSF-MRI Grant (No.1429563), NSF KY EPSCoR RSP Grant and WKU Research Foundation RCAP I Award. K.S. research was supported by the Foundation for Polish Science.

References

(1) Hiramatsu, M.; Hori, M. *Carbon Nanowalls*; Springer Vienna: Vienna, 2010.
(2) Wu, Y.; Qiao, P.; Chong, T.; Shen, Z. Carbon Nanowalls Grown by Microwave Plasma Enhanced Chemical Vapor Deposition. *Adv. Mater.* **2002**, *14*, 64–67.
(3) Hiramatsu, M.; Shiji, K.; Amano, H.; Hori, M. Fabrication of Vertically Aligned Carbon Nanowalls Using Capacitively Coupled Plasma-Enhanced Chemical Vapor Deposition Assisted by Hydrogen Radical Injection. *Appl. Phys. Lett.* **2004**, *84*, 4708.
(4) Chul Shin, S.; Yoshimura, A.; Matsuo, T.; Mori, M.; Tanimura, M.; Ishihara, A.; Ota, K.; Tachibana, M. Carbon Nanowalls as Platinum Support for Fuel Cells. *J. Appl. Phys.* **2011**, *110*, 104308.

(5) González, Z.; Vizireanu, S.; Dinescu, G.; Blanco, C.; Santamaría, R. Carbon Nanowalls Thin Films as Nanostructured Electrode Materials in Vanadium Redox Flow Batteries. *Nano Energy* **2012**, *1*, 833–839.
(6) Hung, T.-C.; Chen, C.-F.; Whang, W.-T. Deposition of Carbon Nanowall Flowers on Two-Dimensional Sheet for Electrochemical Capacitor Application. *Electrochem. Solid-State Lett.* **2009**, *12*, K41–K44.
(7) Stratakis, E.; Giorgi, R.; Barberoglou, M.; Dikonimos, T.; Salernitano, E.; Lisi, N.; Kymakis, E. Three-Dimensional Carbon Nanowall Field Emission Arrays. *Appl. Phys. Lett.* **2010**, *96*, 043110.
(8) Giorgi, L.; Makris, T. D.; Giorgi, R.; Lisi, N.; Salernitano, E. Electrochemical Properties of Carbon Nanowalls Synthesized by HF-CVD. *Sens. Actuators B Chem.* **2007**, *126*, 144–152.
(9) Luais, E.; Boujtita, M.; Gohier, A.; Tailleur, A.; Casimirius, S.; Djouadi, M. A.; Granier, A.; Tessier, P. Y. Carbon Nanowalls as Material for Electrochemical Transducers. *Appl. Phys. Lett.* **2009**, *95*.
(10) Shao, Y.; Wang, J.; Wu, H.; Liu, J.; Aksay, I. A.; Lin, Y. Graphene Based Electrochemical Sensors and Biosensors: A Review. *Electroanalysis* **2010**, *22*, 1027–1036.
(11) Luo, Z.; Shang, J.; Lim, S.; Li, D.; Xiong, Q.; Shen, Z.; Lin, J.; Yu, T. Modulating the Electronic Structures of Graphene by Controllable Hydrogenation. *Appl. Phys. Lett.* **2010**, *97*, 233111.
(12) Patil, A. J.; Vickery, J. L.; Scott, T. B.; Mann, S. Aqueous Stabilization and Self-Assembly of Graphene Sheets into Layered Bio-Nanocomposites Using DNA. *Adv. Mater.* **2009**, *21*, 3159–3164.
(13) Kovalenko, I.; Bucknall, D. G.; Yushin, G. Detonation Nanodiamond and Onion-Like-Carbon-Embedded Polyaniline for Supercapacitors. *Adv. Funct. Mater.* **2010**, *20*, 3979–3986.
(14) Wang, Q.; Plylahan, N.; Shelke, M. V.; Devarapalli, R. R.; Li, M.; Subramanian, P.; Djenizian, T.; Boukherroub, R.; Szunerits, S. Nanodiamond Particles/Reduced Graphene Oxide Composites as Efficient Supercapacitor Electrodes. *Carbon* **2014**, *68*, 175–184.
(15) Siuzdak, K.; Ficek, M.; Sobaszek, M.; Ryl, J.; Gnyba, M.; Niedziałkowski, P.; Malinowska, N.; Karczewski, J.; Bogdanowicz, R. Boron-Enhanced Growth of Micron-Scale Carbon-Based Nanowalls: A Route toward High Rates of Electrochemical Biosensing. *ACS Appl. Mater. Interfaces* **2017**, *9*, 12982–12992.
(16) Hosu, I. S.; Sobaszek, M.; Ficek, M.; Bogdanowicz, R.; Drobecq, H.; Boussekey, L.; Barras, A.; Melnyk, O.; Boukherroub, R.; Coffinier, Y. Carbon Nanowalls: A New Versatile Graphene Based Interface for Laser Desorption/Ionization-Mass Spectrometry Detection of Small Compounds in Real Samples. *Nanoscale* **2017**.
(17) Gajewski, W.; Achatz, P.; Williams, O. A.; Haenen, K.; Bustarret, E.; Stutzmann, M.; Garrido, J. A. Electronic and Optical Properties of Boron-Doped Nanocrystalline Diamond Films. *Phys. Rev. B* **2009**, *79*, 045206.
(18) Bogdanowicz, R.; Fabiańska, A.; Golunski, L.; Sobaszek, M.; Gnyba, M.; Ryl, J.; Darowicki, K.; Ossowski, T.; Janssens, S. D.; Haenen, K.; *et al.* Influence of the Boron Doping Level on the Electrochemical Oxidation of the Azo Dyes at Si/BDD Thin Film Electrodes. *Diam. Relat. Mater.* **2013**, *39*, 82–88.
(19) Sobaszek, M.; Skowroński, Ł.; Bogdanowicz, R.; Siuzdak, K.; Cirocka, A.; Zięba, P.; Gnyba, M.; Naparty, M.; Gołuński, Ł.; Płotka, P. Optical and Electrical Properties of Ultrathin Transparent Nanocrystalline Boron-Doped Diamond Electrodes. *Opt. Mater.* **2015**, *42*, 24–34.

(20) Lagrange, J.-P.; Deneuville, A.; Gheeraert, E. A Large Range of Boron Doping with Low Compensation Ratio for Homoepitaxial Diamond Films. *Carbon* **1999**, *37*, 807–810.
(21) Wang, X. H.; Ma, G.-H. M.; Zhu, W.; Glass, J. T.; Bergman, L.; Turner, K. F.; Nemanich, R. J. Effects of Boron Doping on the Surface Morphology and Structural Imperfections of Diamond Films. *Diam. Relat. Mater.* **1992**, *1*, 828–835.
(22) Tan, C.; Rodríguez-López, J.; Parks, J. J.; Ritzert, N. L.; Ralph, D. C.; Abruña, H. D. Reactivity of Monolayer Chemical Vapor Deposited Graphene Imperfections Studied Using Scanning Electrochemical Microscopy. *ACS Nano* **2012**, *6*, 3070–3079.
(23) Davies, T. J.; Moore, R. R.; Banks, C. E.; Compton, R. G. The Cyclic Voltammetric Response of Electrochemically Heterogeneous Surfaces. *J. Electroanal. Chem.* **2004**, *574*, 123–152.
(24) Bogdanowicz, R.; Sobaszek, M.; Ryl, J.; Gnyba, M.; Ficek, M.; Gołuński, Ł.; Bock, W. J.; Śmietana, M.; Darowicki, K. Improved Surface Coverage of an Optical Fibre with Nanocrystalline Diamond by the Application of Dip-Coating Seeding. *Diam. Relat. Mater.* **2015**, *55*, 52–63.
(25) Zhu, W.; Inspektor, A.; Badzian, A. R.; McKenna, T.; Messier, R. Effects of Noble Gases on Diamond Deposition from Methane-hydrogen Microwave Plasmas. *J. Appl. Phys.* **1990**, *68*, 1489–1496.
(26) Butler, J. E.; Oleynik, I. A Mechanism for Crystal Twinning in the Growth of Diamond by Chemical Vapour Deposition. *Philos. Trans. R. Soc. Lond. Math. Phys. Eng. Sci.* **2008**, *366*, 295–311.
(27) Rayar, M.; Veis, P.; Foissac, C.; Supiot, P.; Gicquel, A. Gas Temperature Determination Using BH (0–0) A 1 Π → X 1 Σ + Emission Spectrum in a B 2 H 6 Containing Plasma for Doped Diamond Deposition. *J. Phys. Appl. Phys.* **2006**, *39*, 2151.
(28) Cheesman, A.; Harvey, J. N.; Ashfold, M. N. R. Computational Studies of Elementary Steps Relating to Boron Doping during Diamond Chemical Vapour Deposition. *Phys. Chem. Chem. Phys.* **2005**, *7*, 1121–1126.
(29) Wu, Y.; Yang, B.; Zong, B.; Sun, H.; Shen, Z.; Feng, Y. Carbon Nanowalls and Related Materials. *J. Mater. Chem.* **2004**, *14*, 469–477.
(30) Hiramatsu, M.; Hori, M. Fabrication of Carbon Nanowalls Using Novel Plasma Processing. *Jpn. J. Appl. Phys.* **2006**, *45*, 5522.
(31) Shang, N. G.; Papakonstantinou, P.; McMullan, M.; Chu, M.; Stamboulis, A.; Potenza, A.; Dhesi, S. S.; Marchetto, H. Catalyst-Free Efficient Growth, Orientation and Biosensing Properties of Multilayer Graphene Nanoflake Films with Sharp Edge Planes. *Adv. Funct. Mater.* **2008**, *18*, 3506–3514.
(32) Truscott, B. S.; Kelly, M. W.; Potter, K. J.; Ashfold, M. N. R.; Mankelevich, Y. A. Microwave Plasma-Activated Chemical Vapor Deposition of Nitrogen-Doped Diamond. II: CH4/N2/H2 Plasmas. *J. Phys. Chem. A* **2016**, *120*, 8537–8549.
(33) Yiming, Z.; Larsson, F.; Larsson, K. Effect of CVD Diamond Growth by Doping with Nitrogen. *Theor. Chem. Acc.* **2014**, *133*, 1432.
(34) Tuinstra, F.; Koenig, J. L. Raman Spectrum of Graphite. *J. Chem. Phys.* **1970**, *53*, 1126–1130.
(35) Nemanich, R. J.; Solin, S. A. First- and Second-Order Raman Scattering from Finite-Size Crystals of Graphite. *Phys. Rev. B* **1979**, *20*, 392–401.
(36) Vidano, R.; Fischbach, D. B. New Lines in the Raman Spectra of Carbons and Graphite. *J. Am. Ceram. Soc.* **1978**, *61*, 13–17.
(37) Cuesta, A.; Dhamelincourt, P.; Laureyns, J.; Martínez-Alonso, A.; Tascón, J. M. D. Raman Microprobe Studies on Carbon Materials. *Carbon* **1994**, *32*, 1523–1532.

(38) Kurita, S.; Yoshimura, A.; Kawamoto, H.; Uchida, T.; Kojima, K.; Tachibana, M.; Molina-Morales, P.; Nakai, H. Raman Spectra of Carbon Nanowalls Grown by Plasma-Enhanced Chemical Vapor Deposition. *J. Appl. Phys.* **2005**, *97*, 104320.
(39) Susi, T.; Pichler, T.; Ayala, P. X-Ray Photoelectron Spectroscopy of Graphitic Carbon Nanomaterials Doped with Heteroatoms. *Beilstein J. Nanotechnol.* **2015**, *6*, 177–192.
(40) Ficek, M.; Sankaran, K. J.; Ryl, J.; Bogdanowicz, R.; Lin, I.-N.; Haenen, K.; Darowicki, K. Ellipsometric Investigation of Nitrogen Doped Diamond Thin Films Grown in Microwave CH4/H2/N2 Plasma Enhanced Chemical Vapor Deposition. *Appl. Phys. Lett.* **2016**, *108*, 241906.
(41) Ryl, J.; Burczyk, L.; Bogdanowicz, R.; Sobaszek, M.; Darowicki, K. Study on Surface Termination of Boron-Doped Diamond Electrodes under Anodic Polarization in H2SO4 by Means of Dynamic Impedance Technique. *Carbon* **2016**, *96*, 1093–1105.
(42) Wang, B. B.; Zheng, K.; Gao, D.; Levchenko, I.; Ostrikov, K.; Keidar, M.; Zou, S. S. Plasma-Chemical Synthesis, Structure and Photoluminescence Properties of Hybrid Graphene Nanoflake–BNCO Nanowall Systems. *J. Mater. Chem. C* **2016**, *4*, 9788–9797.
(43) Bogdanowicz, R.; Sawczak, M.; Niedzialkowski, P.; Zieba, P.; Finke, B.; Ryl, J.; Karczewski, J.; Ossowski, T. Novel Functionalization of Boron-Doped Diamond by Microwave Pulsed-Plasma Polymerized Allylamine Film. *J. Phys. Chem. C* **2014**, *118*, 8014–8025.
(44) V. Macpherson, J. A Practical Guide to Using Boron Doped Diamond in Electrochemical Research. *Phys. Chem. Chem. Phys.* **2015**, *17*, 2935–2949.
(45) Min Tan, S.; Ling Poh, H.; Sofer, Z.; Pumera, M. Boron-Doped Graphene and Boron-Doped Diamond Electrodes: Detection of Biomarkers and Resistance to Fouling. *Analyst* **2013**, *138*, 4885–4891.
(46) McCreery, R. L. Advanced Carbon Electrode Materials for Molecular Electrochemistry. *Chem. Rev.* **2008**, *108*, 2646–2687.
(47) Ramesham, R. Cyclic Voltammetric Response of Boron-Doped Homoepitaxially Grown Single Crystal and Polycrystalline CVD Diamond. *Sens. Actuators B Chem.* **1998**, *50*, 131–139.
(48) Luais, E.; Boujtita, M.; Gohier, A.; Tailleur, A.; Casimirius, S.; Djouadi, M. A.; Granier, A.; Tessier, P. Y. Carbon Nanowalls as Material for Electrochemical Transducers. *Appl. Phys. Lett.* **2009**, *95*, 014104.
(49) Krivenko, A. G.; Komarova, N. S.; Stenina, E. V.; Sviridova, L. N.; Mironovich, K. V.; Shul'ga, Y. M.; Manzhos, R. A.; Doronin, S. V.; Krivchenko, V. A. Electrochemical Modification of Electrodes Based on Highly Oriented Carbon Nanowalls. *Russ. J. Electrochem.* **2015**, *51*, 963–975.
(50) Komarova, N. S.; Krivenko, A. G.; Stenina, E. V.; Sviridova, L. N.; Mironovich, K. V.; Shulga, Y. M.; Krivchenko, V. A. Enhancement of the Carbon Nanowall Film Capacitance. Electron Transfer Kinetics on Functionalized Surfaces. *Langmuir* **2015**, *31*, 7129–7137.
(51) González, Z.; Vizireanu, S.; Dinescu, G.; Blanco, C.; Santamaría, R. Carbon Nanowalls Thin Films as Nanostructured Electrode Materials in Vanadium Redox Flow Batteries. *Nano Energy* **2012**, *1*, 833–839.
(52) Roy, P. R.; Saha, M. S.; Okajima, T.; Ohsaka, T. Electrocatalytic Oxidation of Ascorbic Acid by [Fe(CN)6]3−/4− Redox Couple Electrostatically Trapped in Cationic N,N-Dimethylaniline Polymer Film Electropolymerized on Diamond Electrode. *Electrochimica Acta* **2006**, *51*, 4447–4454.
(53) Yang, N.; Uetsuka, H.; Osawa, E.; Nebel, C. E. Vertically Aligned Nanowires from Boron-Doped Diamond. *Nano Lett.* **2008**, *8*, 3572–3576.

(54) Pleskov, Y. V.; Krotova, M. D.; Elkin, V. V.; Varnin, V. P.; Teremetskaya, I. G. Characterization of CVD Diamond Thin Film Electrodes in Terms of Their Semiconductivity. *Electrocatalysis* **2013**, *4*, 241–244.
(55) Singh, K. P.; Bhattacharjya, D.; Razmjooei, F.; Yu, J.-S. Effect of Pristine Graphene Incorporation on Charge Storage Mechanism of Three-Dimensional Graphene Oxide: Superior Energy and Power Density Retention. *Sci. Rep.* **2016**, *6*.
(56) Latto, M. N.; Riley, D. J.; May, P. W. Impedance Studies of Boron-Doped CVD Diamond Electrodes. *Diam. Relat. Mater.* **2000**, *9*, 1181–1183.
(57) Shrestha, N. K.; Schmuki, P. Chapter 3:Electrochemistry at TiO2 Nanotubes and Other Semiconductor Nanostructures. In; 2013; pp. 87–131.
(58) Ramesham, R. Determination of Flatband Potential for Boron Doped Diamond Electrode in 0.5 M NaCl by AC Impedance Spectroscopy. *Thin Solid Films* **1998**, *322*, 158–166.
(59) Gomes, W. P.; Vanmaekelbergh, D. Impedance Spectroscopy at Semiconductor Electrodes: Review and Recent Developments. *Electrochimica Acta* **1996**, *41*, 967–973.
(60) Yang, Y.; Tian, C.; Wang, J.; Sun, L.; Shi, K.; Zhou, W.; Fu, H. Facile Synthesis of Novel 3D Nanoflower-like CuxO/Multilayer Graphene Composites for Room Temperature NOx Gas Sensor Application. *Nanoscale* **2014**, *6*, 7369–7378.
(61) Tongay, S.; Schumann, T.; Miao, X.; Appleton, B. R.; Hebard, A. F. Tuning Schottky Diodes at the Many-Layer-Graphene/Semiconductor Interface by Doping. *Carbon* **2011**, *49*, 2033–2038.
(62) Fang, J.; Vandenberghe, W. G.; Fischetti, M. V. Microscopic Dielectric Permittivities of Graphene Nanoribbons and Graphene. *Phys. Rev. B* **2016**, *94*, 045318.
(63) Krysova, H.; Vlckova-Zivcova, Z.; Barton, J.; Petrak, V.; Nesladek, M.; Cigler, P.; Kavan, L. Visible-Light Sensitization of Boron-Doped Nanocrystalline Diamond through Non-Covalent Surface Modification. *Phys. Chem. Chem. Phys.* **2014**, *17*, 1165–1172.
(64) Tan, R.; Wu, D.; Xu, S.; Zhu, Y.; Xiong, D.; Wang, L.; Yang, P.; Chu, P. K. Electrochemical Characteristics of Nano-Graphene on a Macroporous Electrically Conductive Network Prepared by Hydrothermal Carbonization. *Electrochimica Acta* **2016**, *215*, 515–524.
(65) Bott, A. W. Electrochemistry of Semiconductors. *Curr. Sep.* **1998**, *17*, 87–92.
(66) Sarswat, P. K.; Bhattacharyya, D.; Free, M. L.; Misra, M. Augmented Z Scheme Blueprint for Efficient Solar Water Splitting System Using Quaternary Chalcogenide Absorber Material. *Phys. Chem. Chem. Phys.* **2016**, *18*, 3788–3803.
(67) Pelskov, Y. V.; Sakharova, A. Y.; Krotova, M. D.; Bouilov, L. L.; Spitsyn, B. V. Photoelectrochemical Properties of Semiconductor Diamond. *J. Electroanal. Chem. Interfacial Electrochem.* **1987**, *228*, 19–27.
(68) Sakharova, A. Y.; Pleskov, Y. V.; Quarto, F. D.; Piazza, S.; Sunseri, C.; Teremetskaya, I. G.; Varnin, V. P. Synthetic Diamond Electrodes: Photoelectrochemical Investigation of Undoped and Boron-Doped Polycrystalline Thin Films. *J. Electrochem. Soc.* **1995**, *142*, 2704–2709.
(69) Wang, Y.; Kececi, K.; Velmurugan, J.; Mirkin, M. V. Electron Transfer/Ion Transfer Mode of Scanning Electrochemical Microscopy (SECM): A New Tool for Imaging and Kinetic Studies. *Chem. Sci.* **2013**, *4*, 3606–3616.
(70) Bard, A. J.; Faulkner, L. R. *Electrochemical Methods: Fundamentals and Applications*; 2 edition.; Wiley: New York, 2000.

TOC graphic